The Impact of Positron Range on PET Resolution, Evaluated with Phantoms and PHITS Monte Carlo Simulations for Conventional and Non-conventional Radionuclides

L. M. Carter[1], **Adam Leon Kesner**[2], **E. C. Pratt**[1,3], **V. A. Sanders**[4], **A. V. F. Massicano**[5], **C. S. Cutler**[4], **S. E. Lapi**[5], **Jason S. Lewis**[1,3,6,7,8]

[1]Department of Radiology, Memorial Sloan Kettering Cancer Center, New York, NY, USA

[2]Department of Medical Physics, Memorial Sloan Kettering Cancer Center, New York, NY, USA

[3]Department of Pharmacology, Weill Cornell Medical College, New York, NY, USA

[4]Collider-Accelerator Department, Brookhaven National Laboratory, Upton, NY, USA

[5]Department of Radiology, University of Alabama at Birmingham, Birmingham, AL, USA

[6]Molecular Pharmacology Program, Memorial Sloan Kettering Cancer Center, New York, NY, USA

[7]Department of Radiology, Weill Cornell Medical College, New York, NY, USA

[8]Radiochemistry and Molecular Imaging Probes Core, Memorial Sloan Kettering Cancer Center, New York, NY, USA

Abstract

Purpose: The increasing interest and availability of non-standard positron-emitting radionuclides has heightened the relevance of radionuclide choice in the development and optimization of new positron emission tomography (PET) imaging procedures, both in preclinical research and clinical practice. Differences in achievable resolution arising from positron range can largely influence application suitability of each radionuclide, especially in small-ring preclinical PET where system blurring factors due to annihilation photon acollinearity and detector geometry are less significant. Some resolution degradation can be mitigated with appropriate range corrections implemented during image reconstruction, the quality of which is contingent on an accurate characterization of positron range.

Procedures: To address this need, we have characterized the positron range of several standard and non-standard PET radionuclides (As-72, F-18, Ga-68, Mn-52, Y-86, and Zr-89) through imaging of small-animal quality control phantoms on a benchmark preclinical PET scanner. Further, the Particle and Heavy Ion Transport code System (PHITS v3.02) code was utilized for Monte Carlo modeling of positron range-dependent blurring effects.

Results: Positron range kernels for each radionuclide were derived from simulation of point sources in ICRP reference tissues. PET resolution and quantitative accuracy afforded by various radionuclides in practicable imaging scenarios were characterized using a convolution-based method based on positron annihilation distributions obtained from PHITS. Our imaging and simulation results demonstrate the degradation of small animal PET resolution, and quantitative accuracy correlates with increasing positron energy; however, for a specific "benchmark" preclinical PET scanner and reconstruction workflow, these differences were observed to be minimal given radionuclides with average positron energies below ~ 400 keV.

Conclusion: Our measurements and simulations of the influence of positron range on PET resolution compare well with previous efforts documented in the literature and provide new data for several radionuclides in increasing clinical and preclinical use. The results will support current and future improvements in methods for positron range corrections in PET imaging.

Introduction

Positron emission tomography (PET) plays a central role in the molecular imaging landscape due to its high sensitivity, accurate quantification, tomographic readout, and diverse applications. While the positron-emitting 2-deoxy-2-[^{18}F]fluoro-D-glucose largely dominates contemporary clinical PET, PET technology/machines are readily capable of imaging numerous other positron-emitting radionuclides/ radiopharmaceuticals. Different nuclides may have useful chemical/physical/pharmacological characteristics, and modern improvements in radioisotope production methodologies and radiochemistry have made exploration of their use more attractive. In consideration for tracer development, each radionuclide has unique imaging characteristics with respect to image quality, biological vector compatibility, cost, availability, and dosimetry. As we look toward precision imaging of molecular phenotypes, extensive consideration of these factors is warranted. Because PET performance will change with nuclide, it is vital to understand and characterize the variables that will impact image quality. For example, the ability of a nuclear imaging physician to identify molecular and anatomic signatures can directly depend on the resolution and quantitative accuracy provided in the images. Further, the physician must understand the capacity of the images to identify lesions, characterize tumor margins, and/or interpret intratumoral heterogeneity. Thus, as "novel" positron emitters are added to the ensemble of medically relevant radionuclides, their imaging characteristics should be evaluated in comparison with others in current use to enable optimal selection for incorporation into specific PET tracers and applications.

In support of these needs, the present work, in part, characterizes the spatial resolution provided by two nonstandard PET radionuclides, As-72 and Mn-52, which are increasingly utilized in preclinical research. These nonstandard positron emitters are compared with four others, including F-18, Ga-68, Zr-89, and Y-86 which are already integrated in modern clinical practice and have been characterized extensively in phantom imaging studies [1–3]

and Monte Carlo simulations [3–8] in previous literature. Concurrently, our intent is to (a) provide insight into positron range-energy relationships that affect PET spatial resolution *via* 1D, 2D, and 3D visualization and (b) provide kernel documentation to enable future improvements in image reconstruction techniques utilizing positron range correction/point-spread function modeling for improved resolution and image accuracy in PET.

Finally, we expand upon traditional methodology for characterizing positron range by employing a method for fast simulation of PET image resolution with 3D finite element mesh phantoms, which can be applied for modeling PET resolution in systems that are geometrically complicated and materially inhomogeneous, *e.g.*, for determination of recovery coefficients in PET imaging of small animals.

Materials and Methods

Resolution in PET is derivative of three fundamental variables: detector element geometry, annihilation photon acollinearity, and positron range [4]. The first two factors are essentially fixed for a given system and are of less consequence in small-ring, preclinical PET systems. In preclinical PET, positron range is generally considered to be the prevailing resolution limiting factor. Range limits resolution to an extent that depends on the energy of emitted positrons and the media in which they propagate. Therefore, use of different isotopes will support different resolution capacities in a given PET system.

Uncertainties arising from the positron range are fundamental to PET. PET images are generated using the assumption that the distribution of a radiotracer can be derived from coincidence detections, assuming that the emission event occurred across the detection-defined line of response. While this assumption works relatively well and enables PET technology to perform at its capacity, escalating positron energy (and by extension, range) induces degradation of performance as the assumption further breaks down. Upon emission, positron energy is attenuated *via* a protracted sequence of stochastic radiative and collisional energy losses in response to interaction with the transport medium as described in Bethe's theoretical treatment [9]. Generally, when the kinetic energy of the particle is sufficiently dissipated, the positron will pair with an electron and undergo annihilation, producing two coincident, almost collinear 511 keV gamma rays (*i.e.*, the PET signal). For a given decay, the probability an annihilation event occurs at some particular location relative to the source decay event is given by the positron annihilation point spread kernel, *aPSF*. The other primary contributors to resolution degradation, annihilation photon acollinearity, and detector element size may also be mathematically characterized as kernel distributions (*PSF_{acoll}* and *PSF_{geo}*, respectively). The latter kernels are radionuclide independent and depend entirely on the specifics of the imaging system. The overall system point spread function (PSF), *PSF_{sys}*, can be defined as a convolution of these kernels:

$$PSF_{sys} = aPSF \otimes PSF_{acoll} \otimes PSF_{geo} = aPSF \otimes PSF_{scanner} \tag{1}$$

where in the latter portion of Eq. (1), we have combined the radionuclide-independent kernels into single kernel *PSF_{scanner}*. If *aPSF* and *PSF_{scanner}* are adequately characterized, they can be integrated into modern reconstruction algorithms to specifically compensate for

resolution degradation. The inherent difficulty and limited accuracy associated with direct measurement of *aPSF* [10–12] have motivated the use of Monte Carlo transport codes for characterization of the positron range in the more recent literature.

Here, the Particle and Heavy Ion Transport code System (PHITS) [13–16] was used to simulate positron tracks from point sources of activity in relevant tissues, as well as in 3D finite element mesh (FEM) phantoms to mimic PET imaging scenarios commonly encountered in preclinical research. These simulations include imaging of a ubiquitous preclinical phantom archetype used for routine quality control (the Jaszczak/Derenzo-type phantom) and a mouse strain commonly used for preclinical radiotracer development (nude mouse). Moreover, we provide PET images of Jaszczak phantoms filled with solutions of each radionuclide, acquired on a benchmark preclinical PET scanner (Siemens® Inveon™ micro-PET/CT) for comparison and validation of the preclinical simulations and for comparison with previous phantom imaging experiments [10, 11]. A summary of relevant properties for each of the radionuclides examined is provided in Table 1; the positron emission energy spectrum for each radionuclide, obtained from the DECDC nuclear decay database [17], is provided in Fig. 1.

Kernel Characterization and Notation

Historically, the most often-cited distribution utilized for Monte Carlo–based comparisons of positron range blurring effects arising from different radionuclides has not been the density of positron annihilations (*aPSF*) itself, but rather its projection into a single dimension [3–7, 18] (see Fig. 3), *viz*

$$aPSF_{sin}(x) = \int_{-\infty}^{\infty} \int_{-\infty}^{\infty} aPSF_{3D}(x, y, z) \, dz \, dy \qquad (2)$$

where we have adopted the notation of Cal-Gonzalez et al. [14]. In practice, the limits of integration need not be infinite, but must cover the full extent of the positron range. For a point source in an isotropic medium, $aPSF_{3D}(x, y, z)$ reduces to $aPSF_{3D}(r)$ where $r = \sqrt{x^2 + y^2 + z^2}$. The 3D radial density distribution $g_{3D}(r)$ and 3D cumulative probability distribution $G_{3D}(r)$ then follow as

$$g_{3D}(r) = 4\pi r^2 \cdot aPSF_{3D}(r) \qquad (3)$$

$$G_{3D}(r) = \int_0^r g_{3D}(\xi) d\xi \qquad (4)$$

where $\int_r^{r+dr} g_{3D}(\xi) d\xi$ gives the probability of an annihilation occurring between some distance r and $r + dr$ from the origin, and $G_{3D}(r)$ represents the probability of an annihilation occurring within some distance r from the origin. Though due to the spherical symmetry of the present scenario, all of these distributions are ultimately derivable from one another (see Cal-Gonzalez et al. [14]), we have elected to present $G_{3D}(r)$ distributions due to the ease of transformation of these distributions into all others, as well as $aPSF_{sin}(x)$ distributions for ease of comparision with results from previous work.

Isotope Production

Arsenic-72 was obtained as [^{72}As]arsenate from a proprietary ^{72}Se72/^{72}As generator system housed at Brookhaven National Laboratory; the parent Se-72 was produced *via* the ^{75}As(p,4n)^{72}Se nuclear reaction at the Brookhaven Linear Isotope Producer (BLIP) with ~50 MeV protons. Manganese-52 ([^{52}Mn]MnCl$_2$) was produced *via* the ^{Nat}Cr(p,n)^{52}Mn reaction at the University of Alabama at Birmingham cyclotron facility [19]. F-18 was produced as [^{18}F]fluoride *via* ^{18}O(p,n)^{18}F using our in-house GE® PET-trace™ 800 cyclotron at the Radiochemistry and Molecular Imaging Probes (RMIP) core of Memorial Sloan Kettering Cancer Center (MSKCC). Yttrium-86 was produced as [^{86}Y]YCl$_3$ at the MD Anderson Center for Advanced Biomedical Imaging (CABI) cyclotron facility on a GE PETtrace *via* the ^{86}Sr(p,n)^{86}Y reaction. Zirconium-89 was produced *via* the ^{89}Y(p,n)^{89}Zr reaction on the MSKCC RMIP core's EBCO TR19/9 cyclotron. A commercial ^{68}Ge/^{68}Ga generator (Model IGG100; Eckert & Ziegler Radiopharma GmbH, Berlin) provided [^{68}Ga]GaCl$_3$. All radio-isotopes exhibited > 99 % radionuclidic purity at time of production/elution.

Preclinical PET Phantom

A Jaszczak phantom (Data Spectrum® Micro Deluxe Phantom; #ECT/DLX/MMP) was used in the "hot rod" configuration (*i.e.*, using interchangeable insert #ECT/HOTMMP/I); the phantom is comprised of poly(methyl methacrylate), and the insert houses a hexagonal array of sectors containing hollow rods with diameters of 1.2, 1.6, 2.4, 3.2, 4.0, and 4.8 mm, with center-to-center rod spacing equal to twice the rod diameter (Fig. 2a).

Digital Phantoms

Digital finite element mesh (FEM) phantoms, suitable for implementation in Monte Carlo simulations, were developed *ab initio* with computer-aided design software, or, by adaptation from previously published work.

Using manufacturer-specified or measured dimensions of the Jaszczak phantom described previously, a triangulated 3D model of the phantom was constructed in the open-source 3D modeling software Blender™ (Fig. 2b). The uniform section of the digital phantom was truncated to reduce unnecessary computational expense. Additionally, we modified the popular *Digimouse phantom* [20] in Blender™ to mimic a subcutaneous tumor model commonly utilized in preclinical radiopharmaceutical development (Fig. 2c). Specifically, we inserted a spherical lesion (diameter = 5 mm) above the left shoulder as shown.

Following initial design/modification in Blender™, all digital phantoms were converted to a finite element mesh *via* constrained Delaunay tetrahedralization using the mesh generation software TetGen [21]. Material attributes for each mesh component were defined based on ICRP reference atomic compositions obtained from NIST (physics.nist.gov); human/ animal phantoms utilized bone, lung, or soft tissue components where applicable (with densities taken as 1.85 g/cm^3, 1.05 g/cm^3, and 0.30 g/cm^3, respectively), and the Jaszcak phantom was modeled from PMMA (phantom body) and water (radiotracer solution) components.

Monte Carlo Simulations

The PHITS v3.02 was used to model positron transport. Upon initiation, the positrons were assigned an initial energy established *via* sampling the associated positron energy distribution for each radionuclide (Fig. 1) and were assigned a random initial direction vector. The default physics model for positron transport in PHITS were utilized, with in-flight positron annihilation, positrons originating from pair production, and positronium formation/diffusion being ignored in all calculations. A 3 keV kinetic energy threshold was implemented; positrons falling below this threshold were assumed to immediately annihilate and were tallied *via* the [T-Time] tally with output = cutoff.

To characterize positron range, point sources of each radionuclide were simulated in lung, bone, and soft tissues. The 3D positron endpoint distributions were projected onto one dimension (arbitrarily chosen as the *x*-dimension) to derive $aPSF_{sin}(x)$ which was binned in 20-μm increments over the entire sampling volume (Figs. 3 and 4a). For determination of $G_{3D}(r)$ and $g_{3D}(r)$ distributions, the positron endpoints were tallied in regions defined by spheres or spherical shells ($n = 500$ bins) spaced at regular intervals up to the maximum observed positron range. $aPSF_{3D}(r)$ was derived from Eq. (3). In all point source simulations, the sampling volume was chosen as a cube with side lengths of 20 cm, centered at the origin, which allows transport algorithms (always) and binning (where appropriate) to cover the full extent of the positron range.

In the 3D FEM phantoms, source particles were sampled from a spatially uniform distribution within the source reservoirs (*e.g.*, organs, rods). The material beyond the outer surface of each model was defined as void. The mesh grid used for tallying positron endpoints in all preclinical phantom simulations utilized a grid spacing defined to be identical to the voxel dimensions used in PET image reconstruction (*i.e.*, $0.78 \times 0.78 \times 0.80$ mm).

Quantification of Positron Range Kernel

Recalling Eq. (1), the overall system PSF is the convolution of the kernels for positron range, annihilation photon acollinearity, and detector geometry; the 3D PET image volume, then, represents the distribution of the radiotracer, convolved with the overall system PSF. Given only the positron range kernel of Eq. (1) is radionuclide-dependent, and given the mathematical associativity of convolution, we can write

$$\iota_{PET} = \iota_{RT} \otimes PSF_{sys} = \iota_{RT} \otimes aPSF \otimes PSF_{scanner} \tag{5}$$

where ι_{RT} represents the radiotracer distribution and ι_{PET} is the corresponding image as seen by PET. The distribution of positron endpoints is $\iota_{RT} \otimes aPSF$ and is quite simply the raw image volume output by PHITS in our simulations, which we define as ι_{β^+}. The Inveon™ scanner has a manufacturer-specified resolution of 1.4 mm at the center of the field of view (FOV) for images reconstructed using filtered back-projection (FBP), and the resolution has been shown to depend weakly on reconstruction algorithm (FBP *vs.* OSEM2D *vs.* OSEM3D/ MAP) and weakly on radial/tangential positioning near the center of the FOV [22, 23]. We have therefore used the manufacturer-specified value to define

$PSF_{scanner}$ for simulations: specifically, we assume this to take the form of a Gaussian with an isotropic FWHM = 1.4 mm, and further, that its variation within the portion of the scanner's field of view occupied by the subject is small. Thus, we have

$$\iota_{PET} = \iota_{\beta^+} \otimes PSF_{scanner} \qquad (6)$$

or,

$$\iota_{PET}(x, y, z) = \sum_{k = -\infty}^{\infty} \sum_{j = -\infty}^{\infty} \sum_{i = -\infty}^{\infty} \iota_{\beta^+}(i, j, k)$$
$$\cdot \frac{1}{(\sigma\sqrt{2\pi})^3} e^{\left[-\frac{(x-i)^2 + (y-j)^2 + (z-k)^2}{2\sigma^2} \right]} \qquad (7)$$

where

$$\sigma = \frac{FWHM_{scanner}}{2\sqrt{2\ln 2}} \qquad (8)$$

Herein, we simulated PET images through imposition of the convolution expressed in Eq. (5); this Gaussian convolution is implemented in some form in most commercial and open-source 3D image analysis softwares. Importantly, the sampling mesh in our PHITS simulations was chosen so that the voxel dimensions of the volume ι_{β^+}, and by extension ι_{PET}, would match those of the actual images acquired *via* PET, in order to ensure image blur due to voxelization was constant.

PET System Description

PET images were acquired on an Inveon™ hybrid PET/CT (Siemens Medical Solutions®; Knoxville, TN). The PET subsystem employs 64 detector blocks, each housing a 20×20 array of lutetium oxyorthosilicate crystals with dimensions of 1.51 (axial) × 1.51 (transaxial) × 10.0 mm (depth). Each block is coupled through a light guide to a position-sensitive photomultiplier tube. The crystal ring diameter and axial FOV span 16.1 and 12.7 cm, respectively. List mode emission data were sorted into two-dimensional sinograms *via* FORE (span 3, maximum ring difference 79); data were normalized to correct for non-uniform detector response, deadtime count losses, and positron branching ratio, but with no attenuation, scatter, or partial-volume averaging corrections were applied. A 2D ordered subset expectation maximization (OSEM2D; 4 iterations, 16 subsets) was used for reconstruction into $128 \times 128 \times 159$ matrix with $0.78 \times 0.78 \times 0.80$ mm voxel dimensions. All images were visualized in 3D Slicer v4.8.0 (www.slicer.org).

Phantom PET Imaging

The Data Spectrum phantom was filled with an aqueous solution of each radionuclide containing an activity concentration of ~ 10–30 μCi/ml at the time of start of image acquisition. Acquisitions were terminated after 5×10^8 coincident events were detected. A 350–650 keV energy window was utilized for F-18, Ga-68, Zr-89, and Mn-52, while a narrower 450–600 keV window was utilized for Y-86 and As-72 to partially exclude competing gamma emissions; all scans utilized a 3.432-ns coincidence timing window.

Results

Monte Carlo Simulation (Point Source)

Positron transport was simulated from point sources for each radionuclide (1×10^6 total events simulated) in tissues of uniform composition and density, namely, soft tissue, lung tissue, and cortical bone, in order to derive $G_{3D}(r)$ (Fig. 4a, 4b, 4c), $aPSF_{sin}(x)$ (Fig. 4d, 4e, 4f), $g_{3D}(r)$ (Supplementary Figure S2a), and $aPSF_{3D}(r)$ (Supplementary Fig S2b) distributions. The $aPSF_{sin}(x)$ distributions are non-Gaussian and very sharply cusped at the origin. As indicated by former investigators, characterization based on the traditionally used full width at half maximum (FWHM) metric for spatial resolution is inappropriate due to many factors, including the non-Gaussian nature of $aPSF_{sin}(x)$ and the strong dependence of its FWHM on bin size [4, 16]. The full width at 20 % maximum (FW20M) [16] and full width at 10 % maximum (FW10M) [4] of $aPSF_{sin}(x)$ have been suggested as more meaningful measure for gauging resolution losses in PET due to positron range, and we report both here for comparison. Similar to previous work [5–7, 12], $aPSF_{sin}(x)$ for each radionuclide in selected tissues were fit with a two-phase exponential decay (with GraphPad Prism® 7), *viz*

$$N(x) = ae^{-k_1 x} + (1 - a)e^{-k_2 x} \tag{9}$$

where $N(x)$ is number of counts in each 20-μm bin, normalized to maximum counts per bin; the fit parameters are summarized in Table 2. All curve fitting was achieved with $R^2 > 0.99$; FW20M and FW10M values were derived from the fitted curves.

Monte Carlo Simulations (Preclinical QC and Small Animal Phantoms)

Figure 5 provides both Inveon™ PET scanner acquisitions and simulations of each radionuclide in the Data Spectrum® Micro Jaszczak phantom. The positron endpoint tally in each simulated axial slice, and counts per voxel in each PET image slice are normalized to the maximum intensity pixel, and thus, the grayscale lookup scales are directly comparable. $\iota_{RT}(x, y, z) \otimes PSF_{scanner}$ represents the image that would result from an "ideal" PET radionuclide (i.e., zero image blur due to positron range) and is indicative of the combined contributions of voxel sampling and intrinsic scanner resolution, facilitating assessment of the degree of image blur resulting from positron range in the radionuclide-based simulations. Events (5×10^6) were simulated for each radionuclide. Activity profiles for PET images and corresponding simulated images are plotted over the line drawn on the phantom geometry cross section. Table 3 interprets spatial resolution in the Jaszczak phantom images and simulations based on the smallest resolvable rod diameter, determined by operator, similar to clinical QC phantom image analysis methodology.

To estimate isotope dependency of PET resolution in a realistic small animal imaging scenario, we utilized [^{89}Zr]Zr-J591, an anti-prostate-specific membrane antigen monoclonal antibody used previously by our lab [24], as a model biodistribution for comparisons *via* PHITS simulations in our modified *Digimouse* phantom (Fig. 6). For the sake of comparison, it is assumed that biological uptake and clearance of J591 is insensitive to incorporation of a radiolabel and that for short half-life radionuclides, an identical

distribution can be achieved *via*, *e.g.*, pretargeting. Criteria for relative source particle generation in each tissue was defined based on *ex vivo* biodistribution data for [^{89}Zr]Zr-J591 in LNCaP tumor-bearing mice at 96 h post-injection (Table 4). An equivalent number of total positron generation events (1×10^6 events) was simulated for each radionuclide, and thus, it is assumed that specific activity would not be a factor in any case (that is, it is assumed that increased administered activity could be utilized to compensate for low positron emission intensity to achieve similar counting statistics) or, equivalently, that scan times could be prolonged toward the same end. Whole organ mean signal recoveries (mean taken over segment-defined voxel volumes) were quantified from each simulated image volume (Table 4).

Discussion

In this study, we express the implications of PET radioisotope selection on resolution by theoretical and practical characterization. Specifically, we have characterized resolution achievable for six positron-emitting isotopes in a traditional mathematical context by derivation of positron endpoint distributions $aPSF_{sin}(x)$ and $G_{3D}(r)$, and in a practical context *via* simulation of PET images. Though these distributions and simulated images are ultimately unique to each radionuclide studied and should ideally be derived for each use case, the radionuclides investigated span the spectrum of relevant energies of imaging positron emitters and thus allow for relatively easy and accurate interpolation of the results for estimation of imaging performance with other positron-emitting radionuclides not specifically studied here. F-18, Ga-68, and Zr-89 were included in our analysis in particular due to their clinical relevance; the use of Ga-68 in clinics for somatostatin receptor (SSTR2) targeted PET imaging is rapidly expanding due to recent FDA approval of [^{68}Ga]Ga-DOTATATE, and F-18 and Ga-68 remain extremely desirable nuclides for pretargeted imaging of antibodies [25, 26]. Zr-89 remains the preeminent radionuclide for clinical imaging of intact antibodies (*e.g.*, [^{89}Zr]Zr-DFO-trastuzumab, [^{89}Zr]Zr-DFO-5B1), and it as well as clinically utilized Y-86 possesses moderate $\langle E_{\beta+} \rangle$. On the other hand, Mn-52 and As-72 lie at the extremes of the clinically relevant radionuclide spectrum with respect to their average positron energies—Mn-52 is promising for enabling high-resolution PET imaging for intact antibodies [27, 28], while As-72, despite its diminished resolution capacity due to its tremendous positron energy, remains relevant due to its generator-based production and theranostic companionship with As-77 [29].

Comparison with Previous Work

Notable, our use of PHITS differed from previous comparative works which utilized PENELOPE [3, 14, 16] or codes developed in-house [5, 6, 29] for Monte Carlo simulations. A comparison of the results of our simulations with those available in the literature is presented in the Supplementary Information (Fig. S3 and Table S1). Generally, the results of our PHITS simulations agree very well with those of the PENELOPE code, but less so with those of the simulations of Champion et al. [29], which is postulated to be due to the inclusion of modeling of positronium formation and diffusion in the simulations of Champion et al. Spatial binning effects, as well as small differences in the energy spectra, energy binning, transport cutoff energies, and physical models used for positron transport

with each code, ultimately impart some notable differences in results between investigators (*e.g.*, near the origin of the cusp-shaped $aPSF_{sin}(x)$ and $aPSF_{3D}(r)$ distributions), but the effect of these differences on the overall agreement is generally of limited significance. The $G_{3D}(r)$ distribution, owing in part to its nature as a cumulative distribution, is relatively insensitive to the aforementioned effects of binning and simulation parameter setting and is thus well suited for comparison between simulation results, at a size scale relevant in preclinical PET imaging.

Preclinical PET Resolution Degradation with High-Energy Positron Emitters

Despite the potential for increased resolution with, e.g., F-18 and Mn-52 relative to Zr-89 based on their respective median ranges (Table 2), in practice only marginal improvement in image resolution were observed simulations and PET imaging using the Inveon acquisition and reconstruction setting described in the "Materials and Methods" section. These diminished returns largely result from partial volume effects relating to image sampling (voxelization) and limitations stemming from intrinsic scanner resolution. However, for positron emitters more energetic than Zr-89, image quality and quantitative accuracy for small structures rapidly begin to degrade as the contribution of *aPSF* becomes increasingly dominant in the overall system PSF. Nevertheless, in the absence of significant background uptake, the ability to identify small-scale uptake patterns or features (*e.g.*, intrastructure heterogeneity, lymph node uptake) may be largely retained even with high-energy positron emitters including Ga-68 and As-72, though the quantitative accuracy is compromised for small structures (Figs. 5 and 6) in the absence of range corrections.

Fast MC Simulation of PET Image Resolution with PHITS

The convolution-based method for PET image simulation described herein is based on the method of Levin and Hoffman [4], who modeled PET system blurring functions (PSF_{sys}) by convolving Monte Carlo-derived 1D positron range kernels with the kernels for annihilation photon acollinearity and detector geometry; our approach here was, essentially, to extend this to the three-dimensional case, by defining source particle distributions based within 3D finite element models. Such simulations can be applied in a variety of use cases, including determination of signal recovery/recovery coefficients as exemplified in Fig. 6 and Table 4. The method is readily extendable toward modeling performance of any small animal PET system, requiring only knowledge of the intrinsic scanner resolution (which is readily measured or approximated using a point source phantom per the NEMA NU-4 standard), and the distribution of positron annihilation events in the model (which is obtainable with several Monte Carlo codes recently adapted to utilize finite element models, e.g., PHITS, MCNP). In addition, the method is relatively accurate, rapid, and tractable without sophisticated computational infrastructure; most simulations conducted were complete in less than 3 h using a standard PC (2.5-GHz Intel Core i5 processor with 8 GB RAM, running Windows 7 64-bit). It should be noted, however, that certain limitations arise using this approach. As the approach does not implement reconstruction from, *e.g.*, sinogrammed data, reconstruction artifacts observed in true PET images are not reproduced, nor is image noise/ background due to phenomena associated with coincidence detection, *e.g.*, photon scatter and attenuation and random coincidence events. Statistical noise is present in the positron endpoint distributions simulated, but it is suppressed somewhat by convolution with

$PSF_{scanner}$ (this convolution functions as a low pass filter), and thus, fewer positrons must be simulated to achieve acceptable precision. To note, the effects of attenuation and scatter are of secondary importance in preclinical PET imaging using, *e.g.*, mice, and corrections for these effects are rarely performed in this setting; therefore, ignoring these factors in simulation to decrease computation times seems appropriate for the analyses presented here, and further support for this is given by the agreement between the PET and simulated PET images shown in Fig. Fig. 5 which demonstrate that the salient features relating to the *resolution* are appropriately captured. Difference plots of the image pairs in Fig.Fig. 5 are provided in the supplementary information for pixel-level quantitative comparison. We also note, while GEANT4-based GATE PET simulations have evolved to implement sophisticated models for coincidence detection suitable for implementation of reconstruction algorithms, a system-specific assessment of resolution within GATE requires a detailed knowledge of the particular PET system to be simulated (*e.g.*, for appropriate modeling of detector block sizes/geometry), which may or may not be readily available, and the number of decays that must be simulated is many fold higher as-demanded by subsequent reconstruction techniques.

Conclusions

In the present study, we characterized PET resolution provided by a range of preclinically and clinically relevant positron emitters *via* PET imaging of preclinical QC phantoms, and fast Monte Carlo positron transport simulations using PHITS 3.02. Positron range kernels for employment in range correction algorithms in PET image processing are derived. A straightforward and computationally facile method for simulation of PET resolution is utilized for comparisons among different PET radionuclides and is likely to be useful, *e.g.*, for derivation of recovery coefficients for accurate determination of whole organ-level activities in PET/CT imaging based on VOI assessment or for optimizing PET imaging agents through rational isotope selection. The resolution and quantitative accuracy derived from simulation was in strong agreement with complementary images acquired *via* PET scans/reconstruction, and previous research.

Supplementary Material

Refer to Web version on PubMed Central for supplementary material.

Funding Information.

References

1. Laforest R, Liu X (2008) Image quality with non-standard nuclides in PET. Q J Nucl Med Mol Imaging 52:151–158 [PubMed: 18043539]

2. Bunka M, Müller C, Vermeulen C, Haller S, Türler A, Schibli R, van der Meulen NP (2016) Imaging quality of (44)Sc in comparison with five other PET radionuclides using Derenzo phantoms and preclinical PET. Appl Radiat Isot 110:129–133 [PubMed: 26774390]

3. Sanchez-Crespo A (2013) Comparison of gallium-68 and fluorine-18 imaging characteristics in positron emission tomography. Appl Radiat Isot 76:55–62 [PubMed: 23063597]

4. Sánchez-Crespo A, Andreo P, Larsson SA (2004) Positron flight in human tissues and its influence on PET image spatial resolution. Eur J Nucl Med Mol Imaging 31:44–51 [PubMed: 14551751]

5. Levin CS, Hoffman EJ (1999) Calculation of positron range and its effect on the fundamental limit of positron emission tomography system spatial resolution. Phys Med Biol 44:781–799. 10.1088/0031-9155/44/3/019 [PubMed: 10211810]

6. Peng H, Levin CS (2012) Study of PET intrinsic spatial resolution and contrast recovery improvement for PET/MRI systems. Phys Med Biol 57:N101–N115 [PubMed: 22481596]

7. Cal-González J, Herraiz JL, España S, Corzo PMG, Vaquero JJ, Desco M, Udias JM (2013) Positron range estimations with PeneloPET. Phys Med Biol 58:5127–5152 [PubMed: 23835700]

8. Champion C, Loirec CL (2006) Positron follow-up in liquid water: I. A new Monte Carlo track-structure code. Phys Med Biol 51:1707–1723 [PubMed: 16552099]

9. Zur Theorie des Durchgangs schneller Korpuskularstrahlen durch Materie - Bethe - 1930 - Annalen der Physik - Wiley Online Library. https://onlinelibrary.wiley.com/doi/abs/10.1002/andp.19303970303. Accessed 4 Oct 2018

10. Phelps ME, Hoffman EJ, Huang S-C, Ter-Pogossian MM (1975) Effect of positron range on spatial resolution. J Nucl Med 16:649–652 [PubMed: 1151485]

11. Cho ZH, Chan JK, Ericksson L, Singh M, Graham S, MacDonald N, Yano Y (1975) Positron ranges obtained from biomedically important positron-emitting radionuclides. J Nucl Med 16:1174–1176 [PubMed: 1194970]

12. Derenzo SE (1979) Precision measurement of annihilation point spread distributions for medically important positron emitters. Proceedings of the fifth international conference on positron annihilation

13. Sato T, Niita K, Matsuda N, Hashimoto S, Iwamoto Y, Furuta T, Noda S, Ogawa T, Iwase H, Nakashima H, Fukahori T, Okumura K, Kai T, Chiba S, Sihver L (2015) Overview of particle and heavy ion transport code system PHITS. Ann Nucl Energy 82:110–115

14. Sato T, Iwamoto Y, Hashimoto S, Ogawa T, Furuta T, Abe SI, Kai T, Tsai PE, Matsuda N, Iwase H, Shigyo N, Sihver L, Niita K (2018) Features of particle and heavy ion transport code system (PHITS) version 3.02. J Nucl Sci Technol 55:684–690

15. Iwamoto Y, Sato T, Hashimoto S, Ogawa T, Furuta T, Abe SI, Kai T, Matsuda N, Hosoyamada R, Niita K (2017) Benchmark study of the recent version of the PHITS code. J Nucl Sci Technol 54:617–635

16. Furuta T, Sato T, Han MC, Yeom YS, Kim CH, Brown JL, Bolch WE (2017) Implementation of tetrahedral-mesh geometry in Monte Carlo radiation transport code PHITS. Phys Med Biol 62:4798–4810 [PubMed: 28375140]

17. Endo A, Yamaguchi Y (2001) Compilation of new nuclear decay data files used for dose calculation. J Nucl Sci Technol 38:689–696

18. Alva-Sánchez H, Quintana-Bautista C, Martínez-Dávalos A, Ávila-Rodríguez MA, Rodríguez-Villafuerte M (2016) Positron range in tissue-equivalent materials: experimental microPET studies. Phys Med Biol 61:6307–6321 [PubMed: 27494279]

19. Wooten AL, Aweda TA, Lewis BC, Gross RB, Lapi SE (2017) Biodistribution and PET imaging of pharmacokinetics of manganese in mice using manganese-52. PLoS One 12:e0174351 10.1371/journal.pone.0174351 [PubMed: 28306727]

20. Dogdas B, Stout D, Chatziioannou AF, Leahy RM (2007) Digimouse: a 3D whole body mouse atlas from CT and cryosection data. Phys Med Biol 52:577–587 [PubMed: 17228106]

21. Si H (2015) TetGen, a Delaunay-based quality tetrahedral mesh generator. ACM Trans Math Softw 41:11:1–11:36. 10.1145/2629697

22. Disselhorst JA, Boerman OC, Oyen WJG, Slump CH, Visser EP (2010) Spatial resolution of the Inveon small-animal PET scanner for the entire field of view. Nucl Instrum Method A 615:245–248

23. Visser EP, Disselhorst JA, Brom M, Laverman P, Gotthardt M, Oyen WJ, Boerman OC (2009) Spatial resolution and sensitivity of the Inveon small-animal PET scanner. J Nucl Med 50:139–147 [PubMed: 19139188]

24. Holland JP, Divilov V, Bander NH, Smith-Jones PM, Larson SM, Lewis JS (2010) ^{89}Zr-DFO-J591 for immunoPET of prostate-specific membrane antigen expression in vivo. J Nucl Med 51:1293–1300 [PubMed: 20660376]

25. Keinänen O, Fung K, Pourat J, Jallinoja V, Vivier D, Pillarsetty NVK, Airaksinen AJ, Lewis JS, Zeglis BM, Sarparanta M (2017) Pretargeting of internalizing trastuzumab and cetuximab with a ^{18}F-tetrazine tracer in xenograft models. EJNMMI Res 7(95):95 10.1186/s13550-017-0344-6 [PubMed: 29198065]

26. Kraeber-Bodéré F, Rousseau C, Bodet-Milin C et al. (2015) A pretargeting system for tumor PET imaging and radioimmunotherapy. Front Pharmacol 6(54). 10.3389/fphar.2015.00054

27. Graves SA, Hernandez R, Fonslet J, England CG, Valdovinos HF, Ellison PA, Barnhart TE, Elema DR, Theuer CP, Cai W, Nickles RJ, Severin GW (2015) Novel preparation methods of (52)Mn for immunoPET imaging. Bioconjug Chem 26:2118–2124 [PubMed: 26317429]

28. Cox BL, Graves SA, Farhoud M et al. (2016) Development of a novel linearly-filled Derenzo microPET phantom. Am J Nucl Med Mol Imaging 6:199–204 [PubMed: 27508106]

29. DeGraffenreid AJ, Feng Y, Barnes CL et al. (2016) Trithiols and their arsenic compounds for potential use in diagnostic and therapeutic radiopharmaceuticals. Nucl Med Biol 43:288–295 [PubMed: 27150031]
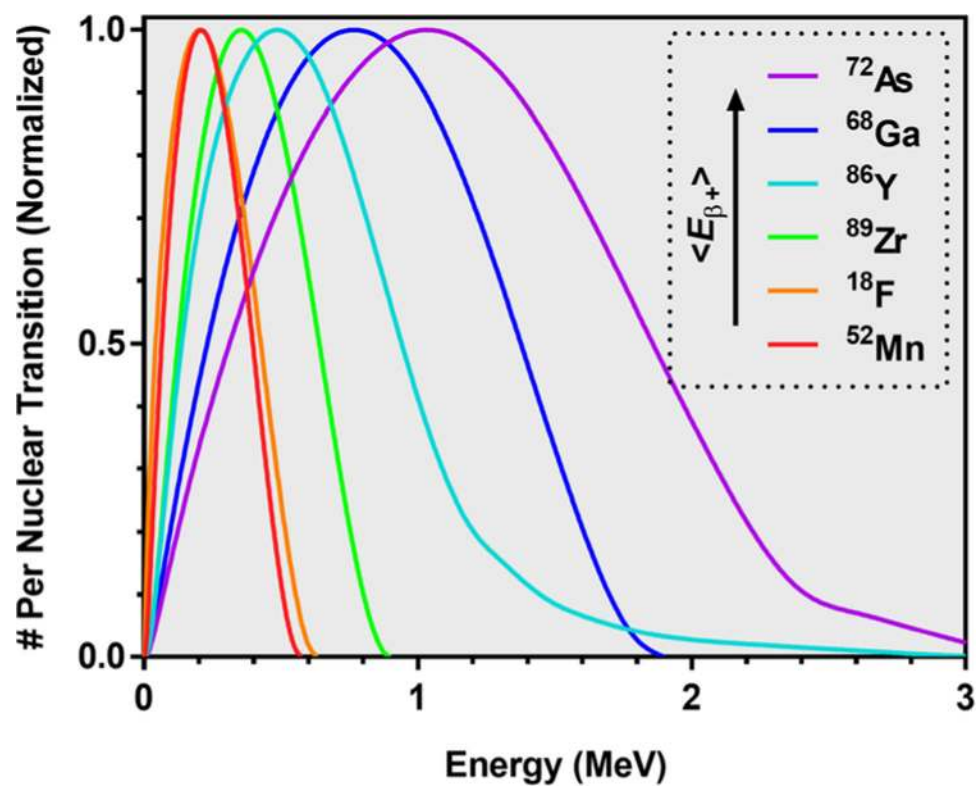
Fig. 1.
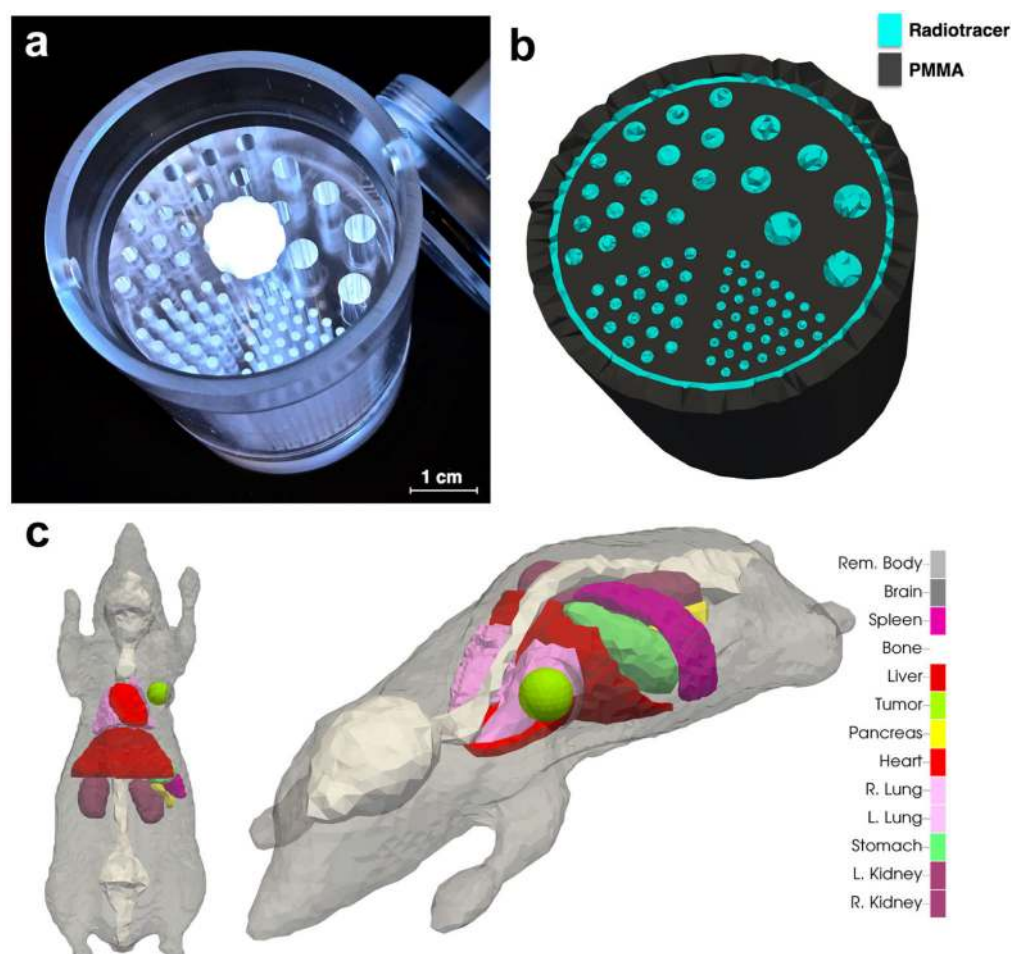Distribution of emitted positrons in energy for each radionuclide examined.

Fig. 2.
Physical and virtual phantoms utilized. **a** Data Spectrum® Micro Deluxe Jaszczak phantom.
b Cross section of FEM version of **a**. **c** *Digimouse* phantom modified with subcutaneous
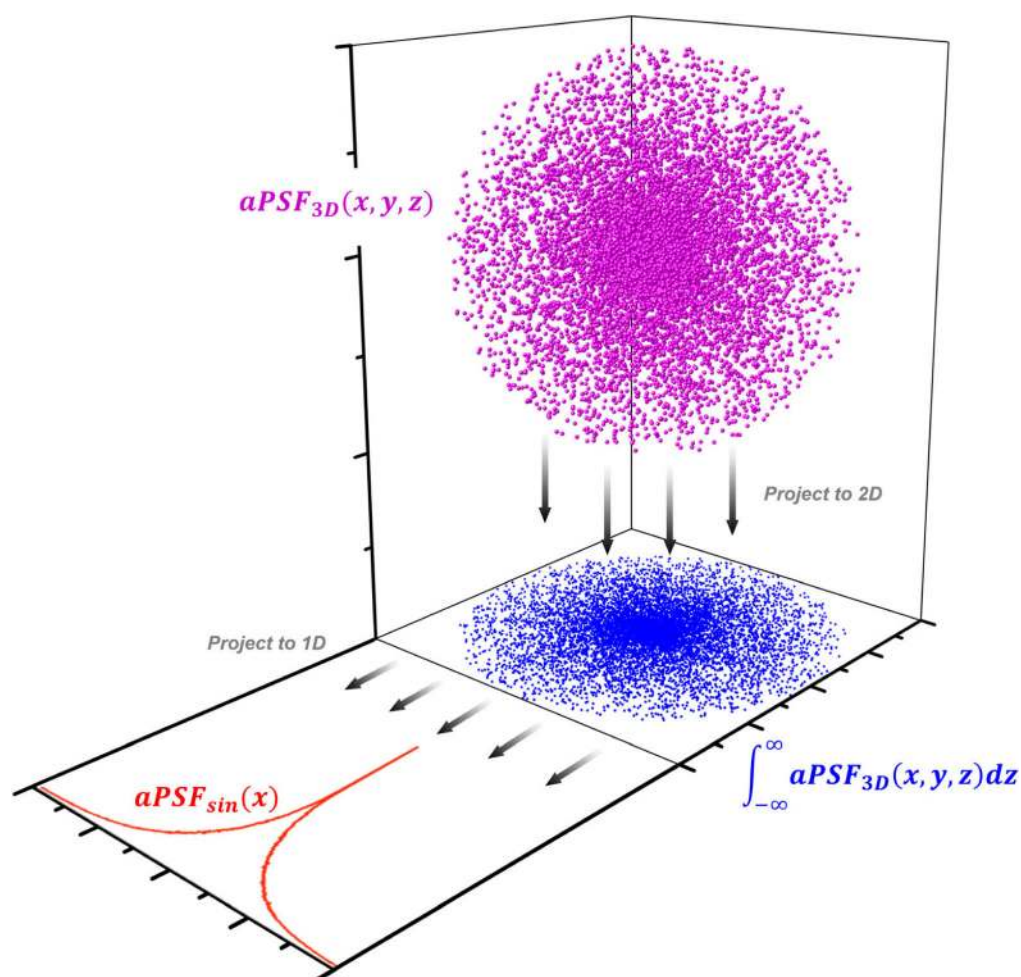shoulder tumor graft.

Fig. 3.
Method for derivation of $aPSF_{sin}(x)$ distribution from a 3D positron endpoint distribution [$aPSF_{3D}(x, y, z)$].
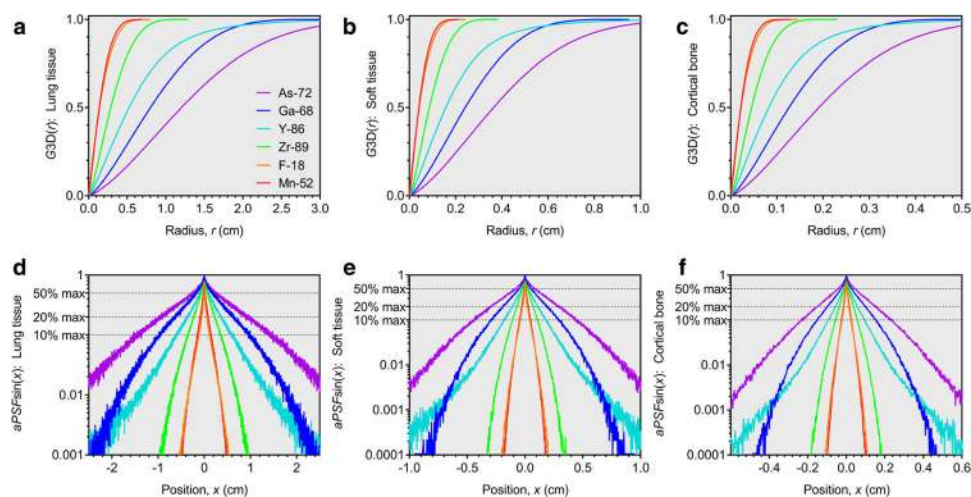
Fig. 4.

$G_{3D}(r)$ distributions in **a** lung tissue, **b** soft tissue, and c cortical bone. $aPSF_{sin}(x)$ distributions in **d** lung tissue, **e** soft tissue, and **f** cortical bone.
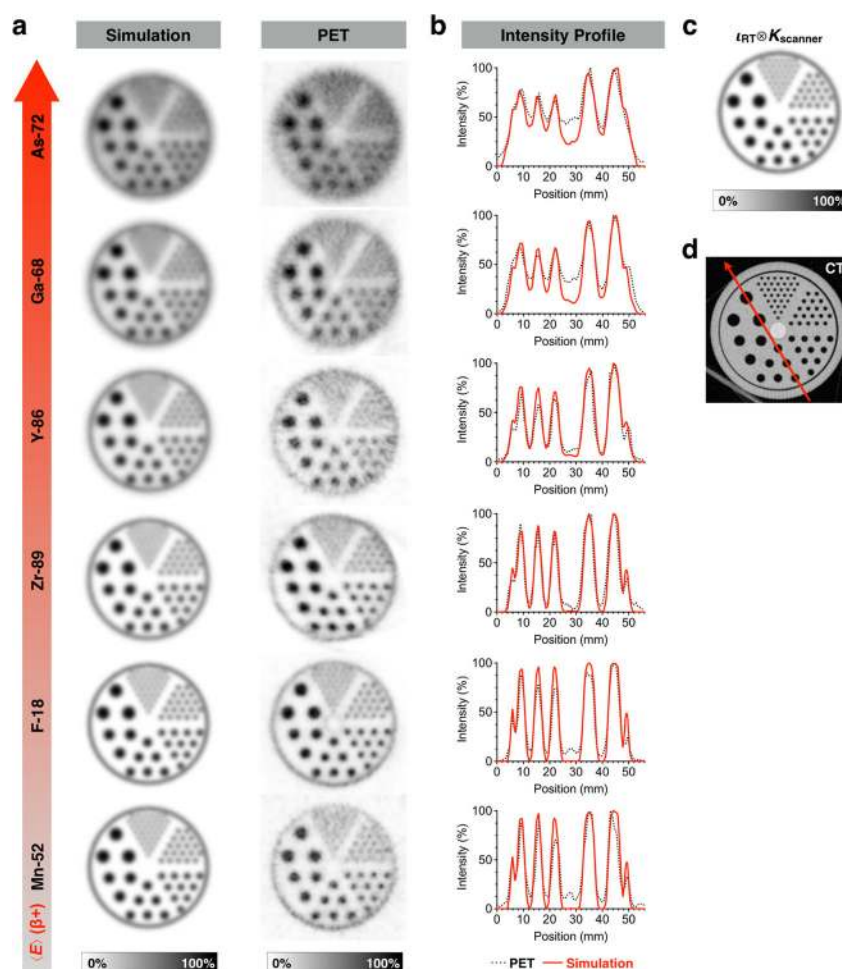
Fig. 5.

a Comparison of PET images and simulations of the Data Spectrum® Micro Jaszczak phantom with different positron emitters. Data are normalized to the maximum pixel intensity in each respective image. **b** Intensity profiles taken over line indicated in **d**. **c** Simulated distribution of radiotracer (*i.e.*, zero positron range blur) convolved with $PSF_{scanner}$ represents upper limit on achievable resolution. **d** Computed tomography (CT) scan of the unfilled Jaszczak phantom.

Fig. 6.
Degradation of resolution and activity recovery for high-energy positron emitters in *simulated* preclinical PET scans of *Digimouse* (coronal slices). Note in particular the poor quantitative accuracy provided by Ga-68 and As-72 for small structures, *e.g.*, tumor, spleen.
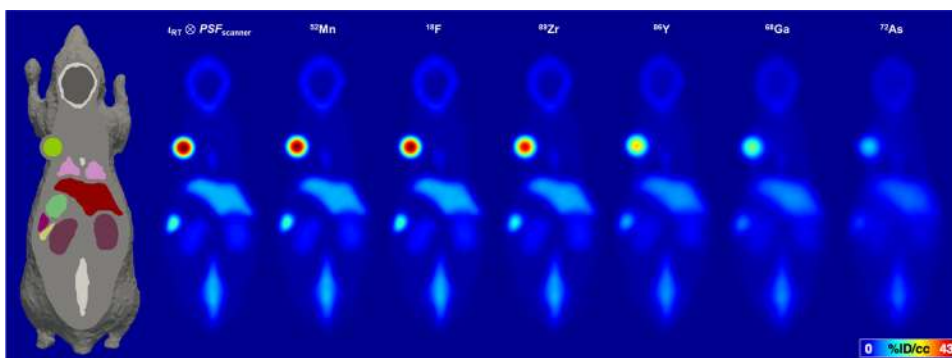
Table 1.

Properties of PET radionuclides examined

Radionuclide	Half-life	$\langle E_{\beta+} \rangle$ (keV)	CDSA range* (cm)	Advantages
^{72}As	26.0 h	1170	0.516	• Intermediate half-life • Generator-based production • High positron intensity (87.8 %) • Theranostic complement (^{77}As)
^{68}Ga	68 min	830	0.337	• Generator-based production • High positron intensity (88.9 %) • Theranostic twins (^{177}Lu, ^{90}Y) • Favorable dosimetric profile for pretargeted immunoPET
^{86}Y	14.7 h	660	0.250	• Theranostic isotopologue (^{90}Y)
^{89}Zr	78.4 h	396	0.123	• Optimal half-life for traditional immunoPET • High resolution
^{18}F	110 min	250	0.062	• High resolution • High positron intensity (96.7 %) • Favorable dosimetric profile • For pretargeted immunoPET
^{52}Mn	5.59 days	242	0.059	• High-resolution immunoPET

*
Range taken in the continuous slowing down approximation (CDSA) in water for the average energy positron emission (data obtained from NIST; physics.nist.gov)

Page 21

Table 2.

Fit parameters of Eq. (7) and calculated values of *FW20M, FW10M, FWHM,* and median range for selected tissues. Values for k_1 and *FWHM* are italicized to reflect their limited suitability for direct comparison with literature data due to strong dependence on binning

Radionuclide	Tissue	a (AU)	k_1 (cm^{-1})	k_2 (cm^{-1})	FWHM (cm)	FW20M (cm)	FW10M (cm)	Median range (cm)
^{72}As	Lung tissue	0.284 ± 0.002	32.0 ± 0.8	1.388 ± 0.004	0.517	1.837	2.834	1.201
	Soft tissue	0.257 ± 0.001	80 ± 1	4.571 ± 0.009	0.1734	0.574	0.8774	0.3638
	Cortical bone	0.267 ± 0.001	134.9 ± 0.1	8.71 ± 0.01	0.08812	0.2982	0.4572	0.1903
^{68}Ga	Lung tissue	0.278 ± 0.002	28.9 ± 0.5	2.067 ± 0.005	0.3586	1.242	1.913	0.8014
	Soft tissue	0.280 ± 0.001	99 ± 1	6.87 ± 0.01	0.1069	0.373	0.575	0.2413
	Cortical bone	0.290 ± 0.001	160 ± 2	13.09 ± 0.02	0.0546	0.1934	0.2994	0.1258
^{86}Y	Lung tissue	0.379 ± 0.002	26.6 ± 0.2	3.072 ± 0.008	0.18496	0.7382	1.1894	0.5235
	Soft tissue	0.371 ± 0.001	82.2 ± 0.5	10.16 ± 0.01	0.05862	0.2254	0.3618	0.1575
	Cortical bone	0.398 ± 0.001	134.3 ± 0.7	19.07 ± 0.03	0.03072	0.1157	0.1883	0.08208
^{89}Zr	Lung tissue	0.279 ± 0.001	44.8 ± 0.5	5.65 ± 0.01	0.1386	0.4538	0.6988	0.2871
	Soft tissue	0.262 ± 0.001	131 ± 1	18.74 ± 0.03	0.04462	0.1394	0.2134	0.0864
	Cortical bone	0.268 ± 0.001	200 ± 1	35.60 ± 0.05	0.02418	0.07294	0.1118	0.04499
^{18}F	Lung tissue	0.602 ± 0.002	188 ± 2	11.74 ± 0.05	0.01574	0.1174	0.2354	0.1412
	Soft tissue	0.560 ± 0.001	360 ± 2	35.97 ± 0.09	0.008466	0.04396	0.08244	0.04232
	Cortical bone	0.5302 ± 0.0008	474 ± 1	65.7 ± 0.1	0.00632	0.02614	0.04706	0.02239
^{52}Mn	Lung tissue	0.440 ± 0.001	108.9 ± 0.7	11.73 ± 0.02	0.03868	0.1756	0.2938	0.1375
	Soft tissue	0.4206 ± 0.0009	255.1 ± 0.9	37.52 ± 0.05	0.01496	0.05678	0.09364	0.04117
	Cortical bone	0.4048 ± 0.0006	363.9 ± 0.8	70.31 ± 0.06	0.00943	0.03122	0.05074	0.02184

Table 3.

Resolution in data Spectrum® Micro Jaszczak phantom with different positron emitters

Radionuclide	Simulation: smallest resolvable rod diameter (mm)	PET imaging: smallest resolvable rod diameter (mm)
^{72}As	1.6	2.4
^{18}F	1.2	1.2
^{68}Ga	1.6	2.4
^{52}Mn	1.2	1.2
^{86}Y	1.6	1.6
^{89}Zr	1.2	1.2

Table 4.

Simulation organ volumes, organ uptake values from Holland et al. used in simulations, and corresponding organ-level mean signal recovery in the modified *Digimouse* phantom, for different radionuclides

Source tissue	Source %ID/cc	Volume (cc)	Whole-organ mean signal recovery (%ID/cc)						
			$I_{RT} \otimes PSF_{scanner}$	^{52}Mn	^{18}F	^{89}Zr	^{86}Y	^{68}Ga	^{72}As
Tumor	42.4	0.06304	29.09	27.84	27.60	24.95	18.65	14.35	9.630
Brain	0.84	0.3651	3.111	3.118	3.124	3.169	3.116	3.103	2.767
Heart	1.79	0.1754	1.654	1.655	1.649	1.668	1.738	1.828	1.978
Kidney (L)	5.36	0.2085	4.698	4.631	4.616	4.454	4.005	3.680	3.197
Kidney (R)	5.36	0.2076	4.669	4.580	4.565	4.380	3.880	3.544	3.038
Liver	11.8	1.059	10.07	9.903	9.873	9.504	8.428	7.757	6.481
Lung (L)	0.66	0.1028	1.090	1.090	1.098	1.205	1.468	1.686	1.720
Lung (R)	0.66	0.1998	1.009	0.9931	0.9974	1.038	1.143	1.230	1.261
Pancreas	0.84	0.01359	2.747	2.948	2.993	3.389	3.661	3.912	3.417
Spleen	25.8	0.1082	15.17	14.38	14.23	12.64	9.497	7.498	5.436
Stomach	0.84	0.1832	1.536	1.640	1.661	1.904	2.477	2.891	3.067
Skeleton	13.7	0.643	7.578	7.404	7.372	6.984	6.005	5.369	4.414
Rem. body	0.84	18.46	1.382	1.382	1.383	1.398	1.407	1.416	1.189